Chapter 32
Grain Porous Structure and Exploitation Properties of Humidity-Sensitive Magnesium Aluminate Spinel-Type Ceramics

H. Klym, I. Hadzaman, O. Shpotyuk, and A. Ingram

32.1 Introduction

Nanostructured functional spinel-based $MgAl_2O_4$ ceramics is considered very interesting material when it comes to applications as active elements for humidity sensors [1–3]. It is established that sensing functionality of these materials is determined largely by the microstructure of ceramics grains, grain boundaries, and pores [4]. These elements are strongly dependent on ceramics sintering route [5]. Therefore, the correlation between sintering temperature of the abovementioned ceramics, its porous structure, and exploitation properties should be carefully taken into account.

The microstructure of ceramics is typically probed with conventional X-ray diffractometry (XRD) and scanning electron microscopy (SEM) and using porosimetry methods [6, 7]. In order to obtain more information on sintering effects in $MgAl_2O_4$ ceramics, the approach should be extended based on new methods of structural characterization. Those include the techniques that yield independent data on phase composition of ceramics bulk and small (1–2 nm) pores corresponding

H. Klym (✉)
Lviv Polytechnic National University, Lviv, Ukraine
e-mail: halyna.i.klym@lpnu.ua

I. Hadzaman
Drohobych State Pedagogical University, Drohobych, Ukraine

O. Shpotyuk
Vlokh Institute of Physical Optics, Lviv, Ukraine

Jan Dlugosz University in Czestochowa, Czestochowa, Poland

A. Ingram
Opole University of Technology, Opole, Poland

O. Fesenko, L. Yatsenko (eds.), *Nanochemistry, Biotechnology, Nanomaterials, and Their Applications*, Springer Proceedings in Physics 214,
https://doi.org/10.1007/978-3-319-92567-7_32

to capillary condensation processes in ceramics. One of such methods is called positron annihilation lifetime (PAL) spectroscopy [8, 9]. This is an experimental technique used to study extended defects and nanosized free-volume entities in solids despite their structural hierarchy [10].

It is well known that exploitation electrical properties of humidity-sensitive elements based on $MgAl_2O_4$ ceramics depend on sorption processes of active materials [11]. Therefore, the actual task appears in relation to modification of porous materials with controlled microstructure, firstly, with large specific surface area, high open porosity, and controlled and optimal pore size distribution [12, 13].

In this work, we present an attempt to investigate grain porous structure of humidity-sensitive $MgAl_2O_4$ and modified MgO-Al_2O_3 ceramics using combined XRD, Hg-porosimetry, and SEM with PAL methods and influence of technological modification on exploitation properties of the studied ceramics.

32.2 Preparation of Magnesium Aluminate Ceramics

The traditional ceramic technology was used for preparation of spinel $MgAl_2O_4$ and MgO-Al_2O_3 ceramics, as was described in greater details elsewhere [14–18]. The samples of ceramics under study were prepared at maximum sintering temperatures T_s of 1200, 1300, and 1400 °C. Total treatment duration was 2 h. For preparation of $MgAl_2O_4$ ceramics, initial fine-dispersed powders of Al_2O_3 with specific surface area of 12.4 m^2/g and MgO with specific surface area of 10.7 m^2/g were used as starting components in conventional ceramics technology route [14].

For preparation of modified MgO-Al_2O_3 ceramics, equimolar amounts of initial powders (Al_2O_3 with specific surface area of 67 m^2/g and $4MgCO_3 \cdot Mg(OH)_2 \cdot 5H_2O$ with specific surface area of 12.8 m^2/g) were mixed in a planetary ball mill for 96 h in an environment with acetone to obtain mixture. The aqueous solution of polyvinyl alcohol was used for obtaining of the molding powder. Bilateral compression was performed in steel molds. After pressing, the samples were sintered also in a furnace at 1200, 1300, and 1400 °C for 2 h [16, 17].

Electrical contacts on the planar surface of all ceramics were formed by screen printing using Ru-contained paste and Pt contacts [19, 20]. Pre-dried layers of paste were sintered at 850 °C with an exposure of 10 min [21, 22].

32.3 Experimental Details

The phase composition of the studied ceramics was determined by XRD method. The XRD patterns were recorded at room temperature using HZG-4a powder diffractometer with Cu$K\alpha$ radiation. This equipment was calibrated with NIST SRM-1976 and Si standards. The measurements were carried out with the 2θ step of 0.05° with variable scanning rate, depending on the sample quality. The profile

analyses were performed using X-ray reflections approximation method by pseudo-Voigt function. The lattice parameters and crystal structures of phases were refined using the Rietveld method [23] and WinPLOTR software [24, 25].

The grain porous structure of ceramics was studied using scanning electron microscopy (SEM) with LEO 982 field emission microscope [14, 16, 17]. The pore size distribution of $MgAl_2O_4$ ceramics in the region from 2 to 1000 nm was studied using Hg-porosimetry (Porosimetr 4000, Carlo Erba Strumentazione) [26, 27].

The PAL measurements with a full width at half maximum of 270 ps were performed with the ORTEC spectrometer using ^{22}Na source placed between two sandwiched samples as it was described in more details elsewhere [14, 16, 28–34]. In order to study the influence of the sintering temperature on the size of nanopores in ceramic bulk, the PALS investigations were performed at 22 °C and RH = 35% after 7 days of exposure in water (vapor in desiccator at RH = 100%) and further drying in vacuum at 120 °C during 4 h. The obtained spectra were analyzed with LT 9.0 computer program [35, 36], and the best fitting results were obtained using four-component fitting procedures. Each of these spectra was processed multiple times owing to slight changes in the number of final channels, annihilation background, and the time shift of the spectrum. Then, the variance of statistically weighted least-squares deviations between experimental points and theoretical curve was taken into account to compare the obtained results. Only the results having deviations close to 1.0 (the optimal deviation typically ranges from 0.95 to ~1.1–1.2 [37]) were selected for further consideration. In such a manner, we obtained numerical PAL parameters (positron lifetimes τ_1, τ_2, τ_3, and τ_4 and intensities I_1, I_2, I_3, and I_4) which correspond to annihilation of positrons in the samples of interest [14, 16, 34].

The positron trapping modes in the studied ceramics were calculated using a known formalism for two-state positron trapping model [9, 38]:

$$\tau_{\text{av.}} = \frac{\tau_1 I_1 + \tau_2 I_2}{I_1 + I_2}, \tau_{\text{b}} = \frac{I_1 + I_2}{\frac{I_1}{\tau_1} + \frac{I_2}{\tau_2}}, \kappa_{\text{d}} = \frac{I_2}{I_1}\left(\frac{1}{\tau_{\text{b}}} - \frac{1}{\tau_2}\right) \tag{32.1}$$

where τ_{b} is positron lifetime in defect-free bulk, $\tau_{\text{av.}}$ is average positron lifetime, and κ_{d} is positron trapping rate of defect. In addition, the $(\tau_2 - \tau_{\text{b}})$ difference was accepted as a size measure for extended free-volume defects where positrons are trapped (in terms of equivalent number of monovacancies), and the τ_2/τ_{b} ratio was taken in a direct correlation to the nature of these defects [39].

Assuming approximately spherical shape of the free volume, the *o-Ps* lifetime (τ_3 and τ_4) in oxide materials can be related to the average radius of pores (R) by semiempirical Tao-Eldrup equation [40, 41]:

$$\tau_{o-Ps} = \left[2\left(1 - \frac{R}{R + \Delta R} + \frac{1}{2\pi}\sin\left(\frac{2\pi R}{R + \Delta R}\right)\right) + 0.007\right]^{-1}, \tag{32.2}$$

where ΔR is the empirically determined parameter (in the classical case $\Delta R \approx$ 0.1656 nm), describing effective thickness of the electron layer responsible for the "pick-off" annihilation of *o-Ps* in the hole [40].

The humidity sensitivity of ceramics was determined by measuring the dependence of electrical resistance R on relative humidity RH of environment. The electrical resistance of the studied ceramics was measured in the heat and humidity chamber PR-3E "TABAI" at 20 °C in the region of RH = 20–99%. The electrodes were attached to the connecting cables of M-Ohmmeter. Electrical measurements were made at fixed frequency of 500 Hz to avoid of polarization of adsorbed water molecules. The maximal overall uncertainties in the electrical measurements did not exceed approximately ±(0.02–0.04) M-Ohm in electrical resistance. The confidence interval in RH measuring bar restricted by equipment accuracy was no worse than ±1%. In addition, the degradation transformation at 40 °C and RH = 95% for 240 h was induced in samples in order to study their stability in time [14, 16, 17].

32.4 Results and Discussion

32.4.1 Spinel $MgAl_2O_4$ Ceramics

With respect to our XRD measurements, the ceramics sintered at 1200 °C has a three-phase composition with the lattice parameter $a = 8.07996(3)$ Å (see Fig. 32.1).

In contrast, the ceramics sintered at 1300 °C contains only two phases, the main spinel-type (lattice parameter $a = 8.0822(2)$ Å) and MgO phases (the remainders of α-Al_2O_3 phase disappear). The ceramics sintered at $T_s = 1400$ °C in addition to the main spinel phase with lattice parameter $a = 8.0828(1)$ Å has a small quantity of MgO phase as compared to the ceramics sintered at $T_s = 1300$ °C (corresponding contents of MgO phase in the above ceramics are 3.48% and 1.54%, respectively) [14]. Thus, it can be concluded that there is a different amount of additional MgO/Al_2O_3 phases in the studied $MgAl_2O_4$ ceramics (see Fig. 32.1 and Table 32.1).

The obtained trimodal pore size distributions of spinel $MgAl_2O_4$ ceramics sintered at 1200, 1300, and 1400 °C are shown in Fig. 32.2. These distributions describe the charge-transferring micropores with radius r_1 depending on sintering conditions, water-exchange inside-delivering or communication mesopores (r_2), and water-exchange outside-delivering macropores (r_3) depending on specific surface area of milled MgO-Al_2O_3 powder [14, 26]. Maximum peak positions (r_1, r_2, and r_3) and intensities (I_{r1}, I_{r2}, and I_{r3}) of the pore size distribution for studied ceramics are summarized in Table 32.2. The obtained results indicate that the sintering temperature influences the porous structure of ceramics. It is shown that the radius of micropores r_1 in $MgAl_2O_4$ ceramics slightly increases from 3.2 nm for samples sintered at 1200 °C to 3.5 nm for ceramics obtained at 1300 °C. Position of the first peak I_{r1} decreases from 5% to 3% for ceramics sintered at 1100–1200 °C and is stabilized at that level in ceramics obtained at 1300–1400 °C (Fig. 32.2b, c).

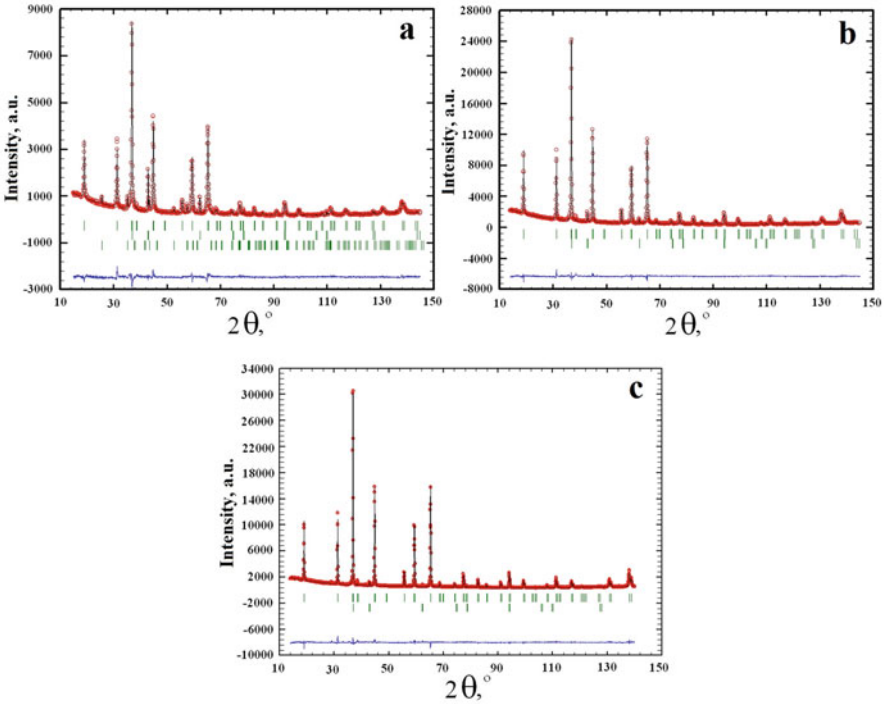

Fig. 32.1 Experimental (rings), theoretical (line), and difference XRD pattern (down) for $MgAl_2O_4$ ceramics sintered at 1200 °C (**a**), 1300 °C (**b**), and 1400 °C (**c**) (row of reflexes is the basic spinel phase)

Table 32.1 Phase compositions of $MgAl_2O_4$ ceramics obtained by XRD method [14]

	Phase composition/space group					
	$MgAl_2O_4/Fd\bar{3}m$		α-$Al_2O_3/R\bar{3}c$		$MgO/Fm\bar{3}m$	
T_s, °C	Lattice parameter, Å	Weight fraction, %	Lattice parameter, Å	Weight fraction, %	Lattice parameter, Å	Weight fraction, %
1200	$a = 8.0796(3)$	88.12	$a = 4.7585(5)$, $c = 12.991(2)$	6.06	$a = 4.2112(2)$	5.82
1300	$a = 8.0822(2)$	96.52	–	–	$a = 4.2114(3)$	3.48
1400	$a = 8.0828(1)$	98.46	–	–	$a = 4.2117(7)$	1.54

The radius r_2 substantially rises from 28 to 97 nm with increasing T_s. The peak width narrows and the intensity I_{r2} is near 2.5–4%. At the same time, the second peak is shifted toward the third peak. Obviously, such changes can be attributed to the expanding of the contact area between grains during the initial stage of sintering. Spherical pores are transformed into cylindrical. Subsequent confluence of these pores is accompanied by diminishing of their surface and volume. There is an intensive growth of grains and forming of a small number of large pores. The radius r_3 slightly rises from 310 to 400 nm with increasing T_s. The intensity of the third peak I_{r3} increases from 11% to 23% [14].

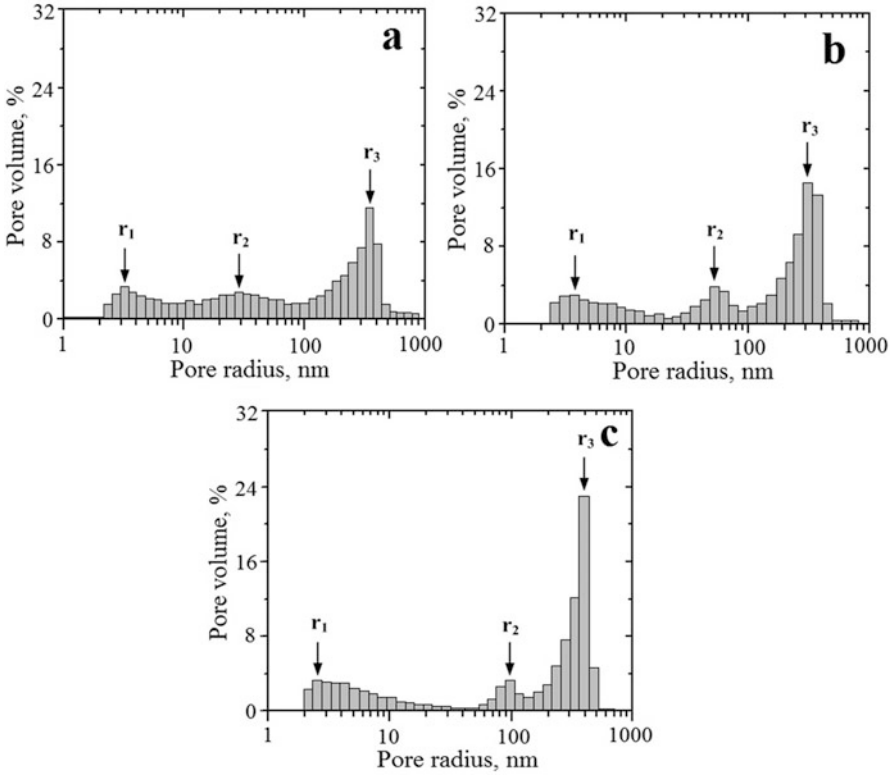

Fig. 32.2 Pore size distributions of $MgAl_2O_4$ ceramics sintered at 1200 °C (**a**), 1300 °C (**b**), and 1400 °C (**c**) [14]

Table 32.2 Peak positions of the pore size distribution for $MgAl_2O_4$ ceramics sintered at 1200–1400 °C [14]

T_c, °C	r_1, nm	I_{r1}, %	r_2, nm	I_{r2}, %	r_3, nm	I_{r3}, %
1200	3.2	3	28	2.5	310	11
1300	3.5	3	43	4	320	15
1400	3.0	3	97	3	400	23

As it follows from visual examination of SEM images shown in Fig. 32.3, the structure of grains in ceramics sintered at 1200 °C is incomplete (Fig. 32.3a). Average grain size is nearly 200 nm. In ceramics sintered at 1300 °C and 1400 °C, the contact region between grains is increased (Fig. 32.3b, c). At that, the grains are integrated into agglomerates. Pores tend to shape into spherical and then cylindrical forms and locate near grain boundaries. Average grain size for these ceramic samples increases to ~300–500 nm. At the same time, the so-called "closed" porosity (not involved in absorption-desorption processes) is formed.

According to Kelvin equation [42, 43], cylindrical pores with radii between 1 and 20 nm are required for capillary condensation of humidity in ceramics at room temperature in the investigated range of RH (20–99%). Such a region includes a

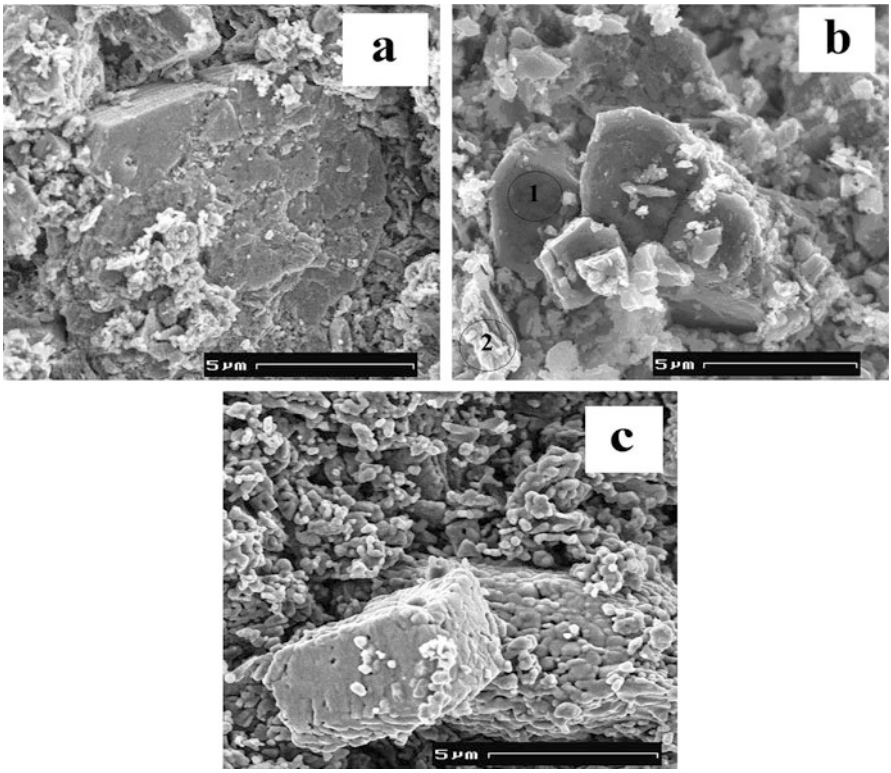

Fig. 32.3 Scanning electron micrographs of $MgAl_2O_4$ ceramics sintered at 1200 °C (**a**), 1300 °C (**b**), and 1400 °C (**c**) [14]

pore distribution peak at r_1 and a secondary peak at r_2. Meso- and macropores with larger radius (>20 nm, the second and the third peak) are not involved in the capillary condensation process, but they ensure the effective transfer of water into ceramic bulk. However, by using traditional porosimetry equipment, we were not able to obtain the information about pores that are smaller than 1–2 nm and other free-volume entities in ceramics. Therefore, alternative methods, such as PAL technique, are needed for the deeper understanding of adsorption/desorption processes in porous materials.

It should be noted that PAL is especially sensitive to tiny intrinsic nanopores and small free-volume entities with geometrical sizes less than ≤20 Å [8] because of the small size of *Ps*. Moreover, a possibility of the *Ps* formation should be taken into account, as it was demonstrated previously for some other kinds of glass-like [44–47] powders and fine-grained porous materials [31, 39]. As confirmed by SEM, a variety of positron trapping sites, such as grain boundaries, intrinsic surfaces of pores, incomplete contacts between some grains with pores of different geometrical sizes and shapes, etc., exist in ceramic samples.

Table 32.3 Fitting parameters for $MgAl_2O_4$ ceramics obtained according to four-component fitting procedure [14]

T_s, °C	τ_1, ns	I_1, a.u.	τ_2, ns	I_2, a.u.	τ_3, ns	I_3, a.u.	τ_4, ns	I_4, a.u.
1200	0.164	0.73	0.443	0.24	2.347	0.011	70.51	0.020
1300	0.155	0.82	0.414	0.16	2.426	0.008	68.74	0.014
1400	0.152	0.88	0.388	0.11	2.504	0.007	62.32	0.008

According to SEM data, the observed phases are nonuniformly distributed within ceramics bulk, being more clearly pronounced near grain boundaries (see Fig. 32.3). These phase extractions serve as specific trapping centers for positrons penetrating ceramics. By using PAL technique in addition to XRD and porosimetry methods, we have made an attempt to study more carefully the chemical characteristics of these extracted phases in $MgAl_2O_4$ ceramics sintered at different T_s. We aim also to estimate the size of nanopores in ceramics bulk, where capillary condensation processes occur.

It has been shown already that for $MgAl_2O_4$ ceramics two of positron annihilation channels should be considered – the positron trapping with shortest τ_1 and middle τ_2 lifetimes and *o-Ps* decaying ("pick-off" annihilation) with the longest τ_3 and τ_4 lifetimes [14, 16].

Assuming the two-state positron trapping model for spinel ceramics [8, 9, 38], four components in the fit of the experimental PAL spectra can be associated with the microstructure peculiarities of the spinel. This microstructure exhibits characteristic octahedral and tetrahedral cation vacancies (τ_1, I_1), positron trapping extended defects located near grain boundaries, and positron traps in the free-volume entities (τ_2, I_2). *O-Ps* decay in the water-filled nanopores of ceramics is described by τ_3, I_3 and τ_4, I_4. Within the formalism of this model, the open volume entities free of the electron density are treated as "defects," while hypothetical structure without these entities is treated as the "defect-free" bulk (represented by τ_b value).

It is shown (see Table 32.3) that the lifetime τ_1 of this first component decreases with T_s, while the intensity I_1 increases in accordance with the amount of the main spinel phase. Smaller τ_1 lifetime reflects more perfect ceramics structure prepared at higher T_s. The second component with τ_2 lifetime is directly related to size of free-volume entity (trapping center) and extended defects near grain boundaries. The intensity I_2 is proportional to the number of such "defects."

Positrons are trapped more strongly in the spinel-type ceramics obtained at lower T_s, as reflected in the values of the middle component of the lifetime spectra. As it follows from Table 32.3, the fitting parameters of this lifetime component (τ_2 and I_2) significantly decrease with T_s. Consequently, the corresponding positron trapping modes of extended defects near grain boundaries will also change (see Table 32.4). Indeed, the values of such parameters as $\tau_{av.}$, τ_b, and ($\tau_2 - \tau_b$) decrease with T_s in good accordance with the amount of MgO/Al_2O_3 phases in

Table 32.4 Positron trapping modes and calculated free volume for $MgAl_2O_4$ ceramics

	Positron trapping modes			Free-volume (nanopores) radius	
T_s, °C	$\tau_{av.}$, ns	τ_b, ns	κ_d, ns^{-1}	R_3, Å	R_4, Å
1200	0.232	0.19	0.94	3.19	18.52
1300	0.197	0.17	0.66	3.25	18.18
1400	0.178	0.16	0.44	3.31	17.01

ceramics. Thus, the size and the number of free-volume entity and extended defects near grain boundaries in $MgAl_2O_4$ ceramics decrease with sintering temperature. The characteristic size of these extended positron traps is close to that of single-double atomic vacancies. Hence, the obtained PAL results agree well with phase composition study of $MgAl_2O_4$ ceramics by XRD method.

The third and the fourth longest components in lifetime spectra are due to the "pick-off" annihilation of *o-Ps* atoms in nanopores. Despite small I_3 intensity, these components cannot be eliminated without significant losses in the quality of the fitting procedure. Similar components were detected in different porous substances with different structural type [39, 48]. It can be surmised that these components are related to predominant *o-Ps* "pick-off" decay in nanopores. The τ_3 lifetime of the third component increases with T_s. At the same time its intensity I_3 decreases. These changes correspond to increased nanopore size and smaller amount of nanopores. But size and amount of smaller nanopores in ceramics bulk decrease with T_s which is manifested in changes of τ_4 lifetime and I_4 intensity.

The radius of free volumes of nanopores in $MgAl_2O_4$ ceramics was calculated using Tao-Eldrup model [40, 41] considering *o-Ps* "pick-off" lifetimes of the third and fourth components with lifetimes τ_3 and τ_4. With increasing of ceramics sintering temperature, the free-volume radius R_3 increases from 3.19 to 3.31 Å and R_4 decreases from ~18.5 Å to 17 Å (Table 32.4). Thus, the $MgAl_2O_4$ ceramics with more perfect structure is characterized by larger nanopores needed for effective capillary condensation process.

Changes caused by different pore size distribution and amount of these pores in all regions were reflected in humidity sensitivity of the studied $MgAl_2O_4$ ceramics. In spite of small amount of transporting pores, ceramics sintered at 1200–1300 °C are characterized by a short linear dependence of electrical resistance R vs. RH with an noticeable hysteresis in absorption-desorption cycles (T_s = 1200–1300 °C). However, after the degradation transformation, these ceramic samples show linear dependences in the region of RH = 30–95% (Fig. 32.4a, b). After 240 h at 40 °C and RH = 95%, the profiles of these dependences are changed and shifted. In ceramics sintered at 1400 °C with optimal pore size distribution and necessary number of nanopores tested by PAL method, the dependence R vs. RH is practically linear in all studied RH regions without hysteresis before and after the degradation transformation [14].

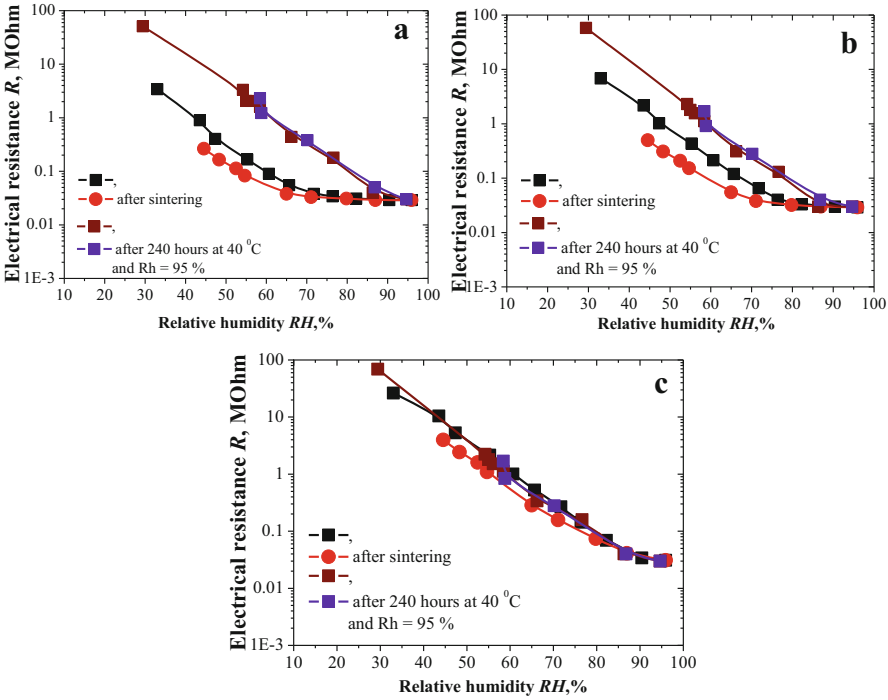

Fig. 32.4 Exploitation properties of $MgAl_2O_4$ ceramics sintered at 1200 °C (**a**), 1300 °C (**b**), and 1400 °C (**c**) [14]

32.4.2 Modified MgO-Al_2O_3 Ceramics

Our results obtained with XRD method testify that ceramics sintered T_s = 1200–1400 °C contain two phases: the main spinel-type $MgAl_2O_4$ phase (space group $Fd\bar{3}m$) and some additives of additional MgO (space group $Fm\bar{3}m$) (see Fig. 32.5). The phase composition and lattice parameter values of MgO-Al_2O_3 ceramics obtained with XRD method are shown in Table 32.5.

Thus, increase in the sintering temperature from 1200 to 1400 °C leads to the formation of spinel phase; the corresponding lattice parameter slightly increases within this process being at the level of 8.08 Å (see Table 32.5). So, we can conclude that in magnesium aluminate ceramics, the same spinel-type phase is formed regardless of T_s like in [14].

The pore size distributions of technologically modified MgO-Al_2O_3 ceramics obtained at 1200, 1300, and 1400 °C are shown in Fig. 32.6. Such distribution covers the charge-transferring nanopores with r_1 radius depending on sintering conditions, water-exchange inside-delivering or communication mesopores (r_2 radius), and water-exchange outside-delivering macropores (r_3 radius) depending on specific surface area of milled MgO-Al_2O_3 powder. Maximum peak positions (r_1, r_2, and

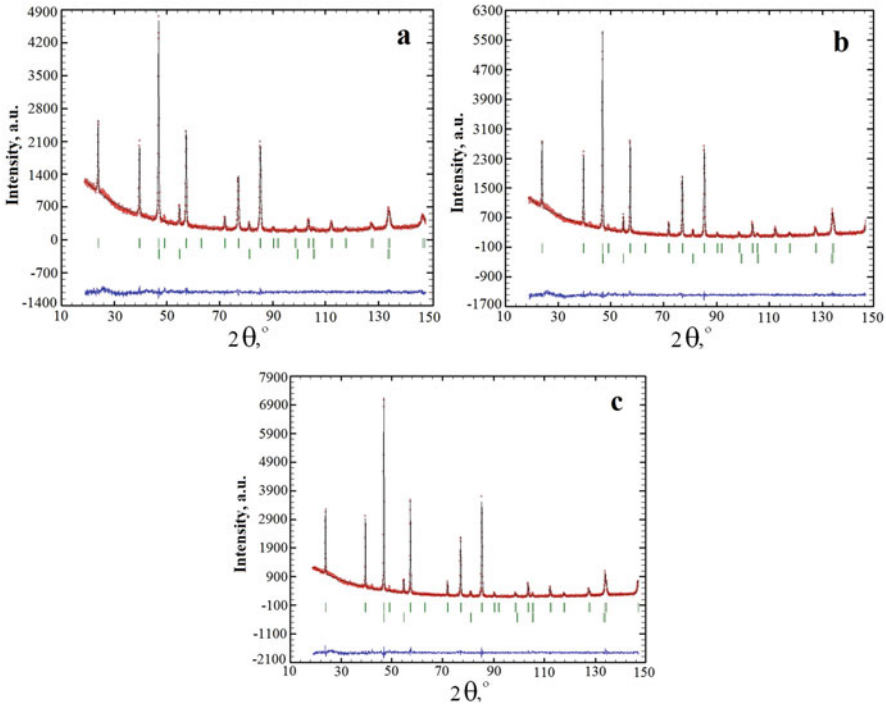

Fig. 32.5 Observed and calculated XRD profiles for MgO-Al_2O_3 ceramics sintered at 1200 °C (**a**), 1300 °C (**b**), and 1400 °C (**c**); the overhead row of reflexes is spinel phase; the lower row of reflexes is MgO phase [16]

Table 32.5 Phase composition of the modified MgO-Al_2O_3 ceramics [16, 17]

	Main $MgAl_2O_4$ phase		Additional MgO phase	
T_c, °C	Lattice parameter, Å	Weight fraction, %	Lattice parameter, Å	Weight fraction, %
1200	8.0809(2)	93.63(0.78)	4.2124(4)	6.37(0.27)
1300	8.0812(2)	94.12(0.80)	4.2145(4)	5.88(0.30)
1400	8.0808(1)	94.05(0.78)	4.2169(4)	5.95(0.34)

r_3) and intensities (I_{r1}, I_{r2}, and I_{r3}) of pore size distribution for studied ceramics prepared at 1200, 1300, and 1400 °C are shown in Table 32.6.

Ceramics sintered at 1200 °C exhibit trimodal pore size distribution with maximum position of r_1, r_2, and r_3 near 2.3, 35, and 160 nm, respectively (Table 32.6 and Fig. 32.6a). It is established that large open pores with size near 100–300 nm correspond to open surface pores in ceramics. They are involved in absorption-desorption process of water from environment. Pores centered near 35 nm are so-called transporting pores providing the effective passing of water into ceramic body [14, 17].

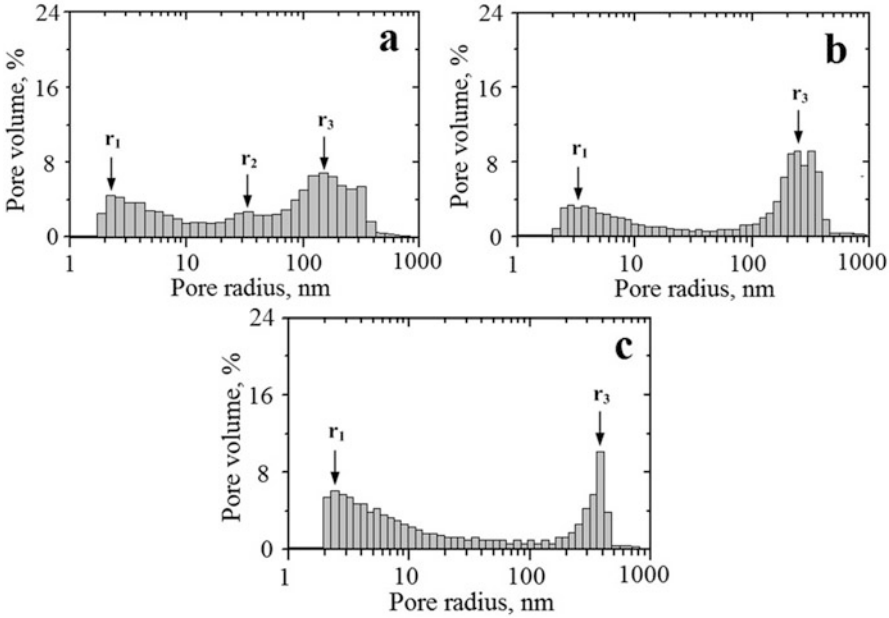

Fig. 32.6 Pore size distributions of MgO-Al_2O_3 ceramics sintered at 1200 °C (**a**), 1300 °C (**b**), and 1400 °C (**c**) [16, 17]

Table 32.6 Peak position of pore size distribution for modified MgO-Al_2O_3 ceramics sintered at 1200–1400 °C

T_c, °C	r_1, nm	I_{r1}, %	r_2, nm	I_{r2}, %	r_3, nm	I_{r3}, %
1200	2.3	4.5	35	3.4	160	6.9
1300	2.9	3.2	–	–	270	9.1
1400	2.5	6.0	–	–	380	10.3

According to Kelvin equation [40, 41], the open cylindrical nanopores with a radius from smaller 1 nm to 20 nm are required for capillary condensation processes of humidity in ceramics at room temperature in the range of relative humidity of 30–98%. Such region includes peak with radius r_1 and partly peak with radius r_2. Meso- and macropores with radius more than 20 nm (the second and the third peak) are not involved in capillary condensation process, but they are needed for effective passing of water into ceramic body.

The obtained results indicate that the sintering temperature influences the porous structure of ceramics. It is shown that radius of nanopores r_1 in studied ceramics slightly increases from 2.3 nm for samples sintered at 1200 °C to 2.9 nm for ceramics obtained at 1300 °C (Fig. 32.6a, b). Intensity of the first peak I_{r1} changes from 4.5% to 3.2% for ceramics sintered at 1200–1300 °C with further growth to 6% in ceramics obtained at 1400 °C (Fig. 32.6c). The position of the second peak with radius r_2 is observed in ceramics sintered at 1200 °C. At the same time, it is shown that this peak is shifted in the direction of the third peak. In ceramics sintered at 1300 and 1400 °C, the clear peak position corresponding to

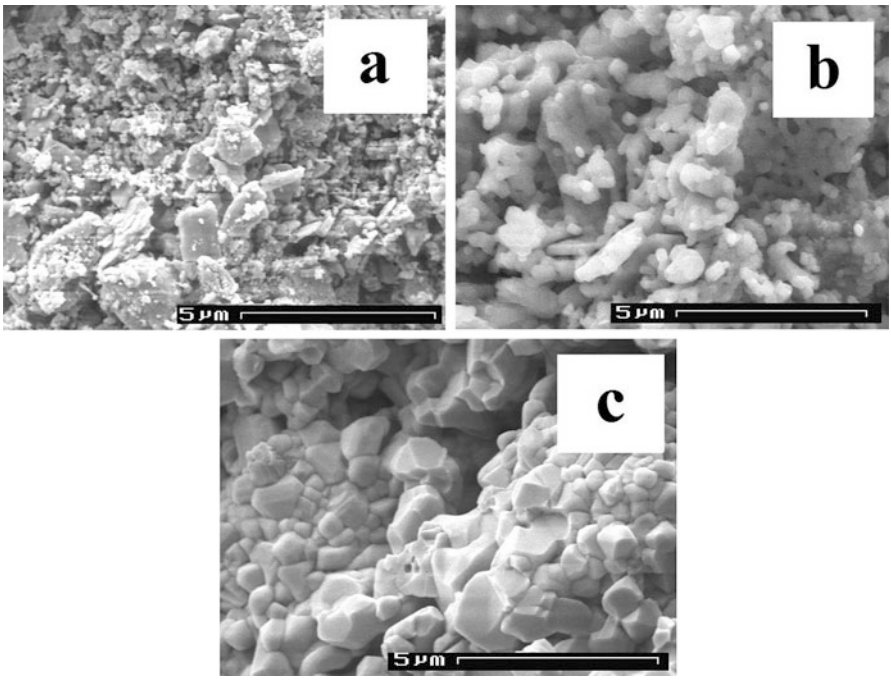

Fig. 32.7 SEM micrograph of the modified MgO-Al_2O_3 ceramics sintered at 1200 °C (**a**), 1300 °C (**b**), and 1400 °C (**c**) [16, 17]

radius r_2 cannot be resolved. But some amount of open mesopores still remains. Thus, trimodal pore size distribution is transformed into bimodal, similarly to [26]. Obviously, such changes can be attributed to the growth of grains during sintering at high temperature with future decreasing of size and amount of pores. Subsequent confluence of pores is accompanied by diminishing of their surface and volume. There occurs an intensive growth of grains and forming of large pores. As a result, the pore size distribution is translocated to macropores region (Fig. 32.6b). Radius r_3 substantially rises from 160 to 380 nm with T_s of ceramics obtained from 1200 to 1400 °C. The intensity I_{r3} of the third peak increases from 6.9% to 10.3% (Table 32.2 and Fig. 32.6b, c).

Evolution of porous structure is confirmed by the results of SEM investigations. It is shown that structure grains and pores in ceramics sintered at 1200 °C are not well formed. Average grain size is about 200 nm. Additional MgO phase is unevenly distributed in the volume of studied ceramics and mostly located near grain boundaries bordering the pores (Fig. 32.7a). With increasing of sintering temperature to 1300 °C, the contact area between grains grows, specific surface area increases, the grains are combined into agglomerates, and the amount of open pores increases. Such pores adopt initially spherical and then cylindrical shapes being located on the grain boundaries (Fig. 32.7b). Average grain size increases to 300–

Table 32.7 Fitting parameters of modified MgO-Al_2O_3 ceramics mathematically treated with four-component fitting procedure

T_c, °C	τ_1, ns	I_1, a.u.	τ_2, ns	I_2, a.u.	τ_3, ns	I_3, a.u.	τ_4, ns	I_4, a.u.
1200	0.16	0.65	0.38	0.33	2.03	0.010	48.4	0.011
1300	0.15	0.67	0.35	0.32	1.98	0.007	40.8	0.005
1400	0.15	0.67	0.35	0.31	1.94	0.008	42.4	0.005

500 nm. These ceramic samples have better developed porosity. Along with this, closed porosity is formed due to the growth of small pores. These closed pores are not involved in the sorption processes in the studied ceramics [17]. In ceramics sintered at 1400 °C, the grain structure continues to take shape showing their intense coagulation. The average size of the grains is near 600–3000 nm. However, the porous structure is modified mainly due to increasing of closed porosity and reduction of channel transport pores (Fig. 32.7c).

As it follows from XRD measurements, the studied MgO-Al_2O_3 ceramics have a different amount of additional MgO phase. In accordance with SEM data, the observed additional phases are nonuniformly distributed within the ceramics bulk, being more clearly pronounced near grain boundaries (see Fig. 32.7). These phase extractions serve as specific trapping centers for positrons penetrating the ceramics. So, by using PAL method, we shall try to study more carefully chemical characteristics of these extracted phases and nanosize free-volume entities (nanopores) in MgO-Al_2O_3 ceramics sintered at different T_s.

As it was shown early, in the case of $MgAl_2O_4$ ceramics, two independent channels of positron annihilation should be considered – the positron trapping with short τ_1 and τ_2 lifetimes and *o-Ps* decaying with longer τ_3 and τ_4 lifetimes.

Taking into account the model described in [8, 9, 38], the shortest lifetime component (the first channel of positron annihilation) in the studied ceramics reflects mainly the microstructure specificity of the spinel with characteristic octahedral and tetrahedral cation vacancies. It is shown (see Table 32.7) that the lifetime τ_1 of this first component slightly decreases with T_s, while the intensity I_1 increases in accordance with the amount of the main spinel phase (see Tables 32.5 and 32.7). Apparently, the decreasing of τ_1 lifetime reflects more perfect ceramics structure prepared at higher T_s. By accepting two-state positron trapping model [38], the longer τ_2 lifetime can be treated as defect-related one, these positron trapping defects being located near grain boundaries [16]. According to our XRD measurements, in the studied MgO-Al_2O_3 ceramics, the amount of additional phases is dependent on T_s (see Table 32.5). Thus, the positrons are trapped more strongly in the spinel-type ceramics obtained at lower T_s, which is reflected in the middle component of lifetime spectra. As it follows from Table 32.3, the fitting parameters of this lifetime component (τ_2 and I_2) significantly decrease with T_s. Consequently, the corresponding positron trapping modes of extended defects near grain boundaries will be changed as well.

Indeed, the values of such parameters as $\tau_{av.}$, τ_b, τ_d, and $(\tau_2 - \tau_b)$ decrease with T_s in good accordance with the amount of additional MgO phase in the studied

Table 32.8 Positron trapping modes and free-volume radius in the modified $MgO\text{-}Al_2O_3$ ceramics

	Free-volume (nanopores) radius		Positron trapping modes				
T_c, °C	R_3, nm	R_4, nm	$\tau_{av.}$, ns	τ_b, ns	κ_d, ns^{-1}	$\tau_2 - \tau_b$, ns	τ_2/τ_b
1200	0.291	1.459	0.24	0.20	1.07	0.18	1.89
1300	0.286	1.328	0.22	0.19	0.85	0.20	2.03
1400	0.282	1.357	0.22	0.19	0.81	0.21	2.10

ceramics (see Table 32.8). But in all cases, the same type of positron trapping center is formed since τ_2/τ_b values are near 2.0. The characteristic size of these extended positron traps near grain boundaries estimated from $(\tau_2 - \tau_b)$ difference is close to single-double atomic vacancies [14].

The third and the fourth longest components in the resolved lifetime spectra are due to "pick-off" annihilation of *o-Ps* atoms in the intergranular pores. It can be surmised that these components are owing to predominant *o-Ps* "pick-off" decaying. The τ_3 and τ_4 lifetimes of these components decrease with T_s. These changes are connected with more branched structure of the open pores of the ceramics sintered at higher T_s (1300 and 1400 °C). With T_s increased, the *o-Ps* "pick-off" decaying occurs preferentially in the nanopores filled by absorbed water, while the ceramic samples sintered at relatively low T_s (1200 °C) show this process in both water-filled and water-free nanopores.

Recently, PAL spectroscopy started to be used as an alternative porosimetry technique to characterize the local free volumes, first of all in both open and closed nanopores. The PAL method is particularly effective when *Ps* is formed. In disordered solids, *Ps* is usually organized in two ground state (*p-Ps* and *o-Ps*) and localized in the pores and free volumes. Usually, quantification is based on the analysis of *o-Ps* lifetime (the lifetimes of the third and fourth components τ_3 and τ_4 in $MgO\text{-}Al_2O_3$ ceramics corresponds to *o-Ps* lifetime). The *o-Ps* "pick-off" annihilation depends on the size of pores and gives additional important information on the void structure of the materials. Despite small I_3 and I_4 intensities for $MgO\text{-}Al_2O_3$ ceramics, it is possible to estimate the average nanopores size from *o-Ps* lifetime in a given material.

In $MgO\text{-}Al_2O_3$ ceramics, there are two *o-Ps*-related PAL components. Therefore, τ_3 and τ_4 lifetimes can be related to corresponding pores via Tao-Eldrup model. The nanopores radii R_3 and R_4 calculated using corresponded $\tau_{o\text{-}Ps}$ values are shown in Table 32.8. The $\tau_{o\text{-}Ps}$ value of around $\sim 40 \div 48$ ns corresponds to nanopores with radius (R_4) distribution centered near $\sim 1.3 \div 1.5$ nm. Most probably, these pores correspond to the empty volumes associated with mismatches in the packing of extended atomic group (clusters, fractals, etc.). The similar lifetime $\tau_3 \approx 2$ ns was also observed in $MgO\text{-}Al_2O_3$ ceramics, and its origin was associated with fine pores of $R_3 \sim 0.3$ nm. Fraction of nanopores associated with *o-Ps* lifetimes can be estimated by the intensities of corresponding long-lived components (I_3 and I_4). However, contrary to the short-lifetime components, annihilating almost entirely via two-quantum annihilation, substantial part of *o-Ps* annihilates also

via three-quantum process, which is completed by the "pick-off" annihilation process [49–51]. Different efficiency of the registration for two- and three-quantum processes can distort the proportion between observed *o-Ps* annihilation intensities (I_3 and I_4) introducing uncertainty into the estimation of the number of pores. In addition, it should be noted that porosimetry methods are limited to open pores, which should have an access to the environment to be determined. These PAL results are complementary data to Hg-porosimetry measurements. On the other hand, PAL spectroscopy can probe both open and closed pores in functional humidity-sensitive ceramics of sizes ranging from atomic scale to several tens of nanometers.

Changes caused by sintering temperature on pore size distribution were reflected in humidity sensitivity of MgO-Al_2O_3 ceramics. Hence, ceramics sintered at low temperature (1200 °C) has enough of open pores in all regions. Such behavior of pore size distribution is manifested in electrical properties of ceramic samples. They have good sensitivity (changes of electrical resistance ~4 orders) between average values of relative humidity (33–95%) and minimal hysteresis of resistance dependence in adsorption-desorption cycles (Fig. 32.8a).

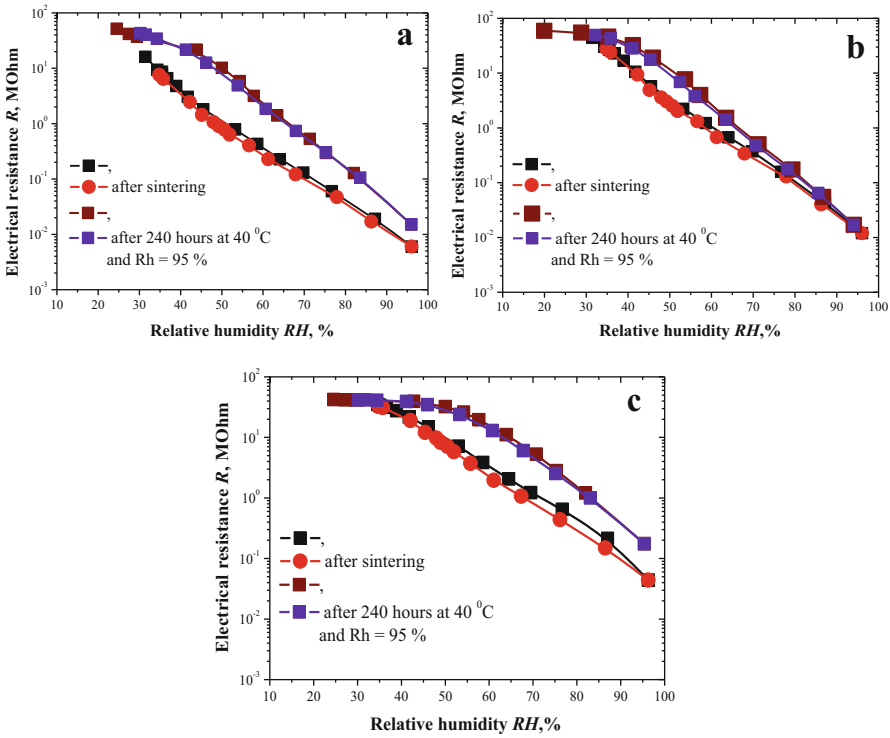

Fig. 32.8 Exploitation properties of the modified MgO-Al_2O_3 ceramics sintered at 1200 °C (**a**), 1300 °C (**b**), and 1400 °C (**c**) [16]

In spite of a small amount of transporting pores, ceramics sintered at 1300 °C are characterized by linear dependence of electrical resistance R vs. RH in the entire studied region without significant hysteresis in absorption-desorption cycles (Fig. 32.8b). But after degradation tests there is a drop in sensitivity down to 35%. However, studied characteristics before and after degradation does not change substantially.

In contrast to other ceramic samples, ceramics sintered at 1400 °C have a small amount of macropores centered near $r_3 = 380$ nm. Humidity sensitivity of these ceramics is characterized by linearity but with appreciable hysteresis (Fig. 32.8c).

Thus, humidity sensitivity in ceramics sintered at low 1200 °C and recoverability of electrical characteristic in adsorption-desorption cycles are obviously connected with sufficient amount of open pores with different size from all pore size distribution region. Increasing of humidity sensitivity and stability of ceramics sintered at 1300°C results in increased amount of open water-exchange outside-delivering macropores. They provide efficient sorption processes of water through small amount of communication mesopores [16, 17].

Bimodal pore size distribution of ceramics sintered at 1400°C continues to be modified. Capillary condensation processes effectively occur due to increasing of amount of transferring nanopores. Hysteresis in absorption-desorption cycles becomes larger due to the reduction of pores with radius r_3.

32.5 Conclusions

It is shown that the structure of humidity-sensitive spinel $MgAl_2O_4$ ceramics is improved with the increase of the sintering temperature, which mainly results in the transformation of the pore size distribution and decreasing of amount of MgO/Al_2O_3 phases located near grain boundaries. Positrons are trapped more intensively in the spinel ceramics obtained at lower temperature. This is reflected in the second component of the lifetime spectra. The third and the fourth longest components of the spectra are due to "pick-off" annihilation of *o-Ps* atoms in nanopores. Tao-Eldrup model can be applied in order to calculate of nanopore size in ceramic materials.

It is established that the sintering temperature allows to change the porous structure of ceramic materials. Evolution of pore size distribution in humidity-sensitive spinel $MgAl_2O_4$ ceramics leads to corresponding changes in water-sorption processes in these materials. Degradation transformations at 40 °C and RH = 95% result in the increased humidity sensitivity of ceramics in all studied regions with minimal hysteresis. Such changes confirm the active work of transporting pores after the full saturation of some nanopores by water is reached.

The sintered temperatures allow to refine the most significant changes in free-volume (porous) structure of modified $MgO\text{-}Al_2O_3$ ceramics and to decrease the amount of additional phases located near grain boundaries. Evolution of pore size distribution from tri- to bimodal in the studied ceramics leads to corresponding

changes in pore-related water-sorption processes. The increase of humidity sensitivity in ceramics sintered at 1300 °C is related to the fact that close to optimal pore size distribution is achieved. It is shown that in all sintered samples there are pores with radii larger than 10–20 nm, which do not participate in the processes of capillary condensation, although their presence is needed to support fast response of humidity-sensitive elements to the change of relative humidity. Positrons are trapped more strongly in the spinel-type ceramics obtained at lower temperature, and this is reflected in the second component of lifetime spectra. The third and the fourth longest components in the resolved lifetime spectra are due to "pick-off" annihilation of *o-Ps* atoms in the intergranular pores. The observed *o-Ps* lifetimes are related to the nanopores with radius of ~0.3 and ~1.3÷1.5 nm based on classic Tao-Eldrup equation. The reported data were confirmed by Hg-porosimetry and SEM results.

Acknowledgment H. Klym thanks the Ministry of Education and Science of Ukraine for its support (grant no. 0116 U004411).

References

1. Zhi C, Chi L (2005) Humidity sensors: a review of materials and mechanisms. Sens Lett 3(4):274–295. https://doi.org/10.1166/sl.2005.045
2. Kulwicki BM (1991) Humidity sensors. J Am Ceram Soc 74(4):697–708. https://doi.org/10.1111/j.1151-2916.1991.tb06911.x
3. Li Y, Fu ZY, Su BL (2012) Hierarchically structured porous materials for energy conversion and storage. Adv Funct Mater 22(22):4634–4667. https://doi.org/10.1002/adfm.201200591
4. Gusmano G, Montesperelli G, Traversa E (1993) Microstructure and electrical properties of $MgAl_2O_4$ thin film for humidity sensors. J Am Ceram Soc 76:743–750. https://doi.org/10.1111/j.1151-2916.1993.tb03669.x
5. Farahani H, Wagiran R, Hamidon MN (2014) Humidity sensors principle, mechanism, and fabrication technologies: a comprehensive review. Sensors 14(5):7881–7939. https://doi.org/10.3390/s140507881
6. Asami K, Mitani S, Fujimori H, Ohnuma S, Masumoto T (1999) Characterization of Co-Al-O magnetic thin films by combined use of XPS. XRD and EPMA Surf Interface Anal 28:250–253. https://doi.org/10.1002/(SICI)1096-9918(199908)28:1<250::AID-SIA587>3.0.CO;2-T
7. Asami K, Ohnuma T (1998) Masumoto XPS and X-ray diffraction characterization of thin Co-Al-N alloy films prepared by reactive sputtering deposition. Surf Interface Anal 26:659–666. https://doi.org/10.1002/(SICI)1096-9918(199808)26:9<659::AID-SIA412>3.0.CO;2-Z
8. Krause-Rehberg R, Leipner HS (1999) Positron annihilation in semiconductors. In: Defect studies. Springer, Berlin/Heidelberg/New York, p 378
9. Shpotyuk O, Filipecki J (2003) Free volume in vitreous chalcogenide semiconductors: possibilities of positron annihilation lifetime study. Wyd-wo WSP w Czestochowie, Czestochowa
10. Hübner C, Staab T, Krause-Rehberg R (1995) On the interpretation of positron-annihilation data in powders and fine-grained materials. Appl Phys A 61(2):203–206. https://doi.org/10.1007/BF01538390
11. Weaver PM, Cain MG, Stewart M, Anson A, Franks J, Lipscomb IP, McBride JP, Zheng D, Swingler J (2012) The effects of porosity, electrode and barrier materials on the conductivity of piezoelectric ceramics in high humidity and dc electric field smart materials and structures. Smart Mater Struct 21(4):045012. https://doi.org/10.1088/0964-1726/21/4/045012

12. Armatas GS, Salmas CE, Louloudi MG, Androutsopoulos P, Pomonis PJ (2003) Relationships among pore size, connectivity, dimensionality of capillary condensation, and pore structure tortuosity of functionalized mesoporous silica. Langmuir 19:3128–3136. https://doi.org/10.1021/la020261h
13. Kashi MA, Ramazani A, Abbasian H, Khayyatian A (2012) Capacitive humidity sensors based on large diameter porous alumina prepared by high current anodization. Sensors Actuators A 174:69–74. https://doi.org/10.1016/j.sna.2011.11.033
14. Klym H, Ingram A, Hadzaman I, Shpotyuk O (2014) Evolution of porous structure and free-volume entities in magnesium aluminate spinel ceramics. Ceram Int 40(6):8561–8567. https://doi.org/10.1016/j.ceramint.2014.01.070
15. Klym H, Ingram A, Shpotyuk O, Hadzaman I, Solntsev V (2016) Water-vapor sorption processes in nanoporous MgO-Al_2O_3 ceramics: the PAL spectroscopy study. Nanoscale Res Lett 11(1):1. https://doi.org/10.1186/s11671-016-1352-6
16. Klym H, Ingram A, Shpotyuk O, Hadzaman I, Hotra O, Kostiv Y (2016) Nanostructural free-volume effects in humidity-sensitive MgO-Al_2O_3 ceramics for sensor applications. J Mater Eng Perform 25(3):866–873. https://doi.org/10.1007/s11665-016-1931-9
17. Klym H, Hadzaman I, Shpotyuk O (2015) Influence of sintering temperature on pore structure and electrical properties of technologically modified MgO-Al_2O_3 ceramics. Mater Sci 21(1):92–95 https://doi.org/10.5755/j01.ms.21.1.5189
18. Klym H, Shpotyuk O, Ingram A, Calvez L, Hadzaman I, Yu K, Ivanusa A, Chalyy D (2017) Influence of free volumes on functional properties of modified chalcogenide glasses and oxide ceramics. Springer Proc Phys 195:479–493. https://doi.org/10.1007/978-3-319-56422-7_36
19. Shpotyuk O, Balitska V, Brunner M, Hadzaman I, Klym H (2015) Thermally-induced electronic relaxation in structurally-modified $Cu_{0.1}Ni_{0.8}Co_{0.2}Mn_{1.9}O_4$ spinel ceramics. Phys B Condens Matter 459:116–121 https://doi.org/10.1016/j.physb.2014.11.023
20. Shpotyuk O, Brunner M, Hadzaman I, Balitska V, Klym H (2016) Analytical description of degradation-relaxation transformations in nanoinhomogeneous spinel ceramics. Nanoscale Res Lett 11(1):499. https://doi.org/10.1186/s11671-016-1722-0
21. Klym H, Balitska V, Shpotyuk O, Hadzaman I (2014) Degradation transformation in spinel-type functional thick-film ceramic materials. Microelectron Reliab 54(12):2843–2848 https://doi.org/10.1016/j.microrel.2014.07.137
22. Hadzaman I, Klym H, Shpotyuk O (2014) Nanostructured oxyspinel multilayers for novel high-efficient conversion and control. Int J Nanotechnol 11(9–10-11):843–853. https://doi.org/10.1504/IJNT.2014.063793
23. Rodriguez-Carvajal J (2001) Recent developments of the program FULLPROF, Commission on Powder Diffraction (IUCr). Newsletter 26:12–19
24. Roisnel T, Rodriguez-Carvajal J (2000) WinPLOTR: a windows tool for powder diffraction patterns analysis, materials, science forum. In: Proceedings of the seventh European powder diffraction conference, Barcelona
25. Hill RJ, Howard CJ (1987) Quantitative phase analysis from neutron powder diffraction data using the Rietveld method. J Appl Crystallogr 20:467–474. https://doi.org/10.1107/S0021889887086199
26. Bondarchuk A, Shpotyuk O, Glot A, Klym H (2012) Current saturation in In_2O_3-SrO ceramics: a role of oxidizing atmosphere. Revista mexicana de física 58(4):313–316. http://www.scielo.org.mx/pdf/rmf/v58n4/v58n4a5.pdf
27. Karbovnyk I, Bolesta I, Rovetskii I, Velgosh S, Klym H (2014) Studies of CdI_2-Bi_3 microstructures with optical methods, atomic force microscopy and positron annihilation spectroscopy. Mater Sci Pol 32(3):391–395. https://doi.org/10.2478/s13536-014-0215-z
28. Klym H, Ingram A, Shpotyuk O, Filipecki J, Hadzaman I (2011) Structural studies of spinel manganite ceramics with positron annihilation lifetime spectroscopy. J Phys Conf Ser 289(1):012010 http://iopscience.iop.org/article/10.1088/1742-6596/289/1/012010/meta
29. Klym H, Ingram A, Shpotyuk O, Filipecki J (2010) PALS as characterization tool in application to humidity-sensitive electroceramics. In: 27th International Conference on Microelectronics Proceedings (MIEL), pp 239–242. https://doi.org/10.1109/MIEL.2010.5490492

30. Shpotyuk O, Filipecki J, Ingram A, Golovchak R, Vakiv M, Klym H, Balitska V, Shpotyuk M, Kozdras A (2015) Positronics of subnanometer atomistic imperfections in solids as a high-informative structure characterization tool. Nanoscale Res Lett 10(1):1–5. https://doi.org/10.1186/s11671-015-0764-z
31. Klym H, Ingram A, Shpotyuk O, Hadzaman I, Solntsev V, Hotra O, Popov AI (2016) Positron annihilation characterization of free volume in micro-and macro-modified $Cu_{0.4}Co_{0.4}Ni_{0.4}Mn_{1.8}O_4$ ceramics. Low Temp Phys 42(7):601–605. https://doi.org/10.1063/1.4959021
32. Filipecki J, Ingram A, Klym H, Shpotyuk O, Vakiv M (2007) Water-sensitive positron-trapping modes in nanoporous magnesium aluminate ceramics. J Phys Conf Ser 79(1):012015. https://doi.org/10.1088/1742-6596/79/1/012015
33. Klym H, Ingram A, Shpotyuk O, Filipecki J, Hadzaman I (2010) Extended defects in insulating $MgAl_2O_4$ ceramic materials studied by PALS methods. IOP Conference Series: Mater Sci Eng 15(1):012044. https://doi.org/10.1088/1757-899X/15/1/012044
34. Klym H, Karbovnyk I, Vasylchyshyn I (2016) Multicomponent positronium lifetime modes to nanoporous study of MgO-Al_2O_3 ceramics. In: 13th international conference on modern problems of radio engineering. Telecommunications and computer science (TCSET), pp 406–408. https://doi.org/10.1109/TCSET.2016.7452071
35. Kansy J (2000) Positronium trapping in free volume of polymers. Rad Phys Chem 58:427–431. https://doi.org/10.1016/S0969-806X(00)00195-X
36. Kansy J (1996) Microcomputer program for analysis of positron annihilation lifetime spectra. Nucl Instrum Methods Phys Res, Sect A 374(2):235–244. https://doi.org/10.1016/0168-9002(96)00075-7
37. Klym HI, Ivanusa AI, Kostiv YM, Chalyy DO, Tkachuk TI, Dunets RB, Vasylchyshyn I (2017) Methodology and algorithm of multicomponent analysis of positron annihilation spectra for nanostructured functional materials. J Nano- Electron Phys 9(3):03037-1-6. https://doi.org/10.21272/jnep.9(3).03037
38. Klym H, Ingram A (2007) Unified model of multichannel positron annihilation in nanoporous magnesium aluminate ceramics. J Phys Conf Ser 79(1):012014. https://doi.org/10.1088/1742-6596/79/1/012014
39. Nambissan PMG, Upadhyay C, Verma HC (2003) Positron lifetime spectroscopic studies of nanocrystalline $ZnFe_2O_4$. J Appl Phys 93:6320. https://doi.org/10.1063/1.1569973
40. Tao SJ (1972) Positronium annihilation in molecular substance. J Chem Phys 56(11):5499–5510. https://doi.org/10.1063/1.1677067
41. Eldrup M, Lightbody D, Sherwood JN (1981) The temperature dependence of positron lifetimes in solid pivalic acid. Chem Phys 63:51–58. https://doi.org/10.1016/0301-0104(81)80307-2
42. Traversa E (1995) Ceramic sensors for humidity detection: the state-of-the-art and future developments. Sensors Actuators 23:135–156. https://doi.org/10.1016/0925-4005(94)01268-M
43. Gusmano G, Montesperelli G, Nunziante P, Traversa E (1993) Microstructure and electrical properties of $MgAl_2O_4$ and $MgFe_2O_4$ spinel porous compacts for use in humidity sensors. Br Ceram Trans 92(3):104–108
44. Klym H, Ingram A, Shpotyuk O (2016) Free-volume nanostructural transformation in crystallized GeS_2–Ga_2S_3–CsCl glasses. Mater Werkst 47(2–3):198–202. https://doi.org/10.1002/mawe.201600476
45. Klym H, Ingram A, Shpotyuk O, Calvez L, Petracovschi E, Kulyk B, Serkiz R, Szatanik R (2015) 'Cold' crystallization in nanostructurized $80GeSe_2$-$20Ga_2Se_3$ glass. Nanoscale Res Lett 10(1):1–8. https://doi.org/10.1186/s11671-015-0775-9
46. Klym H, Ingram A, Shpotyuk O, Karbovnyk I (2016) Influence of CsCl addition on the nanostructured voids and optical properties of 80GeS2-20Ga2S3 glasses. Opt Mater 59:39–42. https://doi.org/10.1016/j.optmat.2016.03.004
47. Klym H, Ingram A, Shpotyuk O, Hotra O, Popov AI (2016) Positron trapping defects in free-volume investigation of Ge-Ga-S-CsCl glasses. Radiat Meas 90:117–121. https://doi.org/10.1016/j.radmeas.2016.01.023

48. Ghosh S, Nambissan PMG, Bhattacharya R (2004) Positron annihilation and Mössbauer spectroscopic studies of in^{3+} substitution effects in bulk and nanocrystaline $MgMn_{0.1}Fe_{1.9\text{-}x}O_4$. Phys Lett A 325:301–308 doi: https://doi.org/10.1016/j.physleta.2004.03.062. Get rights and content
49. Jean YC, Mallon PE, Schrader DM (2003) Principles and application of positron and positronium chemistry. Word Scientific, Singapore
50. Mogensen OE (1995) Positron annihilation in chemistry. Springer, Berlin
51. Nakanishi H, Jean YC, Schrader DM, Jean YC (1998) Positron and positronium chemistry. Elsevier, Amsterdam